Quantum effects in graphitic materials: Colossal magnetoresistance, Andreev reflections, ferromagnetism, and granular superconductivity

N Gheorghiu[1], CR Ebbing[2], BT Pierce[3], and TJ Haugan[3]

[1]UES Inc., Dayton, OH 45432

[2] University of Dayton Research Institute, Dayton, OH 45469

[3]The Air Force Research Laboratory, Wright-Patterson Air Force Base, OH 45433

Nadina.Gheorghiu@yahoo.com

Abstract. Unlike the more common local conductance spectroscopy, nonlocal conductance can differentiate between nontopological zero-energy modes localized around inhomogeneities, and true Majorana edge modes in the topological phase. In particular, negative nonlocal conductance is dominated by the crossed Andreev reflection. Fundamentally, the effect reflects the system's topology. In graphene, the Andreev reflection and the inter-band Klein tunneling couple electron-like and hole-like states through the action of either a superconducting pair potential or an electrostatic potential. We are here probing quantum phenomena in modified graphitic samples. Four-point contact transport measurements at cryogenic to room temperatures were conducted using a Quantum Design Physical Property Measurement System. The observed negative nonlocal differential conductance G_{diff} probes the Andreev reflection at the walls of the superconducting grains coupled by Josephson effect through the semiconducting matrix. In addition, G_{diff} shows the butterfly shape that is characteristic to resistive random-access memory devices. In a magnetic field, the Andreev reflection counters the effect of the otherwise lowered conduction. At low temperatures, the magnetoresistance shows irreversible yet strong giant oscillations that are known to be quantum in nature. In addition, we have found evidence for seemingly granular superconductivity. Thus, graphitic materials show potential for quantum electronics applications, including rectification and topological states.

1. Introduction

While carbon(C)-based materials are known for many practical properties, such as light-weight and high strength, their inner nature is governed by the laws of quantum physics manifested as magnetism [1], conveniently used for spintronics [2], or as unconventional superconductivity [3,4] that we have previously explored [5].

In this paper we present evidence for several quantum phenomena occurring in graphitic materials: nonlinear electronic transport resulting in negative differential resistance, Landau-level quantization, colossal magnetoresistance, ferromagnetism, and Andreev reflections at the boundaries between SC grains and the surrounding semiconducting matrix.

2. Experimental details

The materials are PAN-based (polyacrylonitrile $(CH_2\text{-}CH\text{-}CN)_n$) T300 C fibers (Cytec), highly oriented pyrolytic graphite (particle size 10 μm), and graphite foil (Graphtek). Selected samples were oxygen(O)-ion implanted (Cutting Edge Ions) at 2D concentrations 7.07×10^{12}, 5.66×10^{15}, and 2.24×10^{16} ions/cm^2, respectively. For an ion energy 70 keV, the implantation depth was 125 nm, i.e., $\sim$ 1% implantation volume. The four-wire Van Der Pauw technique was used for resistivity measurements. Scanning electron microscopy pictures and the elemental analysis for fiber samples are shown in Fig. 1.

The quality of the electrical contacts was optically checked using an Olympus BX51 microscope. The current-to-voltage gap ratio was close to the required factor of four [6]. Magneto-transport and magnetization measurements were carried out in the 1.9 K - 300 K temperature range and for magnetic fields of induction B up to 9 T using a Physical Properties Measurement System (PPMS) model 6500 (Quantum Design).
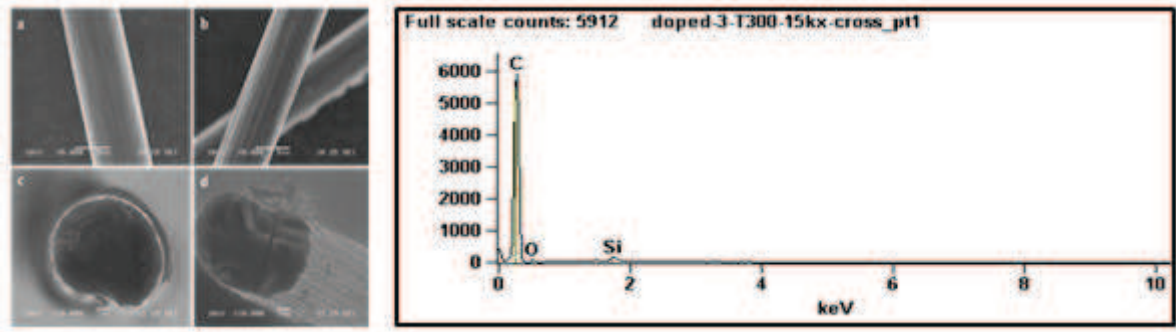

Figure 1 SEM pictures showing the effect of O-ion implantation (2.24×10^{16} ions/cm^2) on the C fiber (b, d) vs. to the raw C fiber (a, c), both along and across the fibers (upper images and lower images, respectively). Also shown are the C and O peaks on the EDS scan. The Si peak is due to the placement of the C fiber on a Si substrate during the implantation procedure. An accelerating voltage of 10.0 kV and a magnification factor ×15000 were used.

3. Results and Discussion

3.1. Electrical resistivity and nonlocal differential conductance without magnetic field

The temperature-dependent resistivity $\rho(T)$ for two C fibers O-implanted at 2.24×10^{16} ions/cm^2 is shown in Fig. 2. At $T \sim 250$ K, there is either an insulator-metal-insulator transition or a metal-insulator-metal transition for a sourced current $I = 20$ μA or $I = 1$ μA, respectively. These transitions reflect the T-dependence balance of charge carrier densities and their mobilities. For the larger I, ρ has a metallic behaviour below $T \sim 25$ K [7]. For the smaller I, ρ for one of the fibers becomes 'negative' for temperatures below ~150 K. The observation of negative resistance (i.e., nonlocal negative voltage) is a signature for highly viscous flow of electrons or, equivalently, zero electrical resistance in the SC state [8]. Moreover, $T \sim 150$ K is the BCS mean-field critical temperature for Cooper-pair instability in graphene [9]. Pseudo-gap behaviour below the onset temperature $T \sim 150$ K is possible.
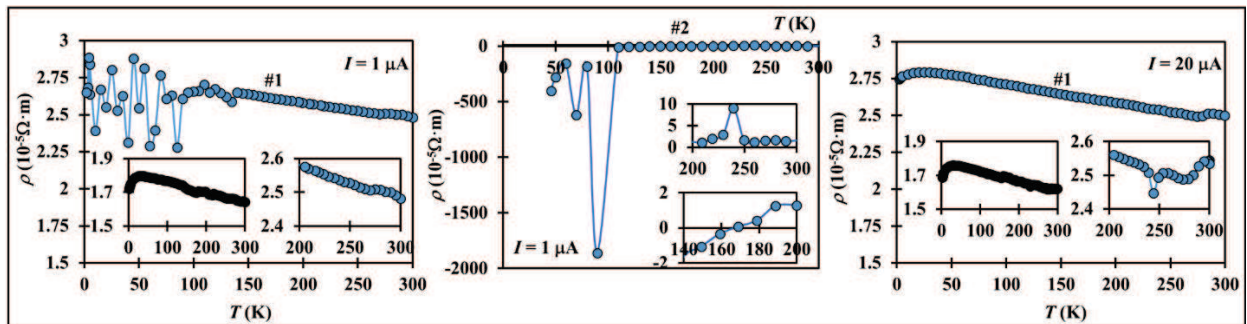

Figure 2 Temperature-dependent electrical resistivity $\rho(T)$ for two C fibers that have been O-implanted at 2.24×10^{16} ions/cm^2 (in blue) and raw fiber (in black), respectively.

Below 150 K, giant fluctuations in the nonlinear differential conductance $G_{diff} = dI/dV$ and the Chua's butterfly are observed at $T = 130$ K (Fig. 3). For $V < 0$, $G_{diff} > 300$ mS or $R_{diff} < 4\ \Omega$ or $\rho_{diff} < 8\ \mu\Omega$·cm. The Chua nonlinear phenomenon can be also seen as a subcritical Hopf bifurcation in which new attractors are being born at the pitchfork point [10]. The inset for $V > 0$ shows that G_{diff} has the shape of the nonlinear $I(V)$ in the Chua circuit. I.e., the charge oscillates as a third-order polynomial of the magnetic flux as in a cubic memristor during a supercritical Andronov–Hopf bifurcation [11]. The butterfly wing span is $\Delta V \cong 0.5$ mV, corresponding to the critical temperature for twisted bilayer graphene, $T_c \cong 1.8$ K. Interestingly, the minimum G_{diff} (< 0) corresponding to $V \cong 60$ mV would give a BCS critical temperature $T_c = 2\Delta/3.53k_B \cong 250$ K, exactly at the insulator-metal transition. The subcritical and supercritical bifurcations meet at the tricritical point and the magnetic field of the local spins acts as a chemical potential. The oxide layer at the surface of the C fiber might be the location of both hard and soft SC fluctuations, i.e., the system might be a multigap SC where the larger gap SC phase takes over the smaller gap SC phases. The evolution of the attractor – which is a manifold of equilibrium states – is actually the evolution of the amplitude (Higgs mode) and phase for the SC order parameter.
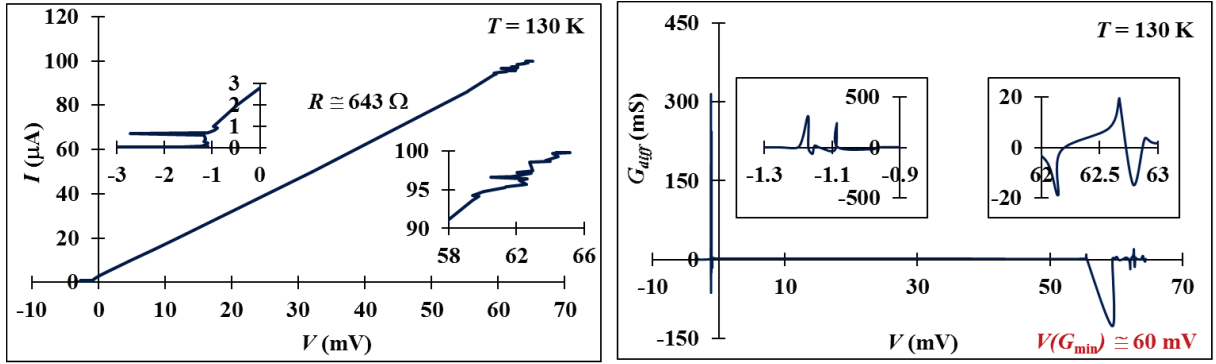

Figure 3 $I(V)$ and the corresponding $G_{diff}(V)$ data for O-implanted (at 2.24×10^{16} ions/cm^2) C fiber.

3.2. Transport measurements in magnetic field
3.2.1 Landau-level quantization, the universal conductance, and butterfly shapes
As known, graphite has antiferromagnetic (AFM) correlations between unlike sublattices (ABAB...) and FM correlations between like sublattices (AAA... or BBB...). A magnetic field can turn a FM into an AFM at the tricritical point, where the FM and AFM merge into the system paramagnetic (PM) phase as the temperature is increased. Under a static magnetic field, the differential resistance $R_{diff} = dV/dI$ (not the voltage-current characteristic $V(I)$) shows the butterfly shape (Figure 4). Significantly, Landau-level quantization results in a G_{diff} peak exactly at the universal conductance $G_0 = 2e^2/h \cong 77$ μS, two peaks at $G_0/4$ (one for $V = 0$), and a minimum due to the Zeeman spin-splitting at $\cong -0.9G_0/2$. Anomalous Josephson effect induced by spin-orbit interaction and Zeeman effect in semiconductor channel between two SC grains is also possible. In a semiconductor nanowire, a $G_0/2$ conductance peak in high enough magnetic field is a signature of ballistic 1D transport, where backscattering is reduced and spin degeneracy is lifted. An even higher magnetic field (normal to the wire) can lead to the depopulation of sub-bands and $G_0/4$ peaks are observed.
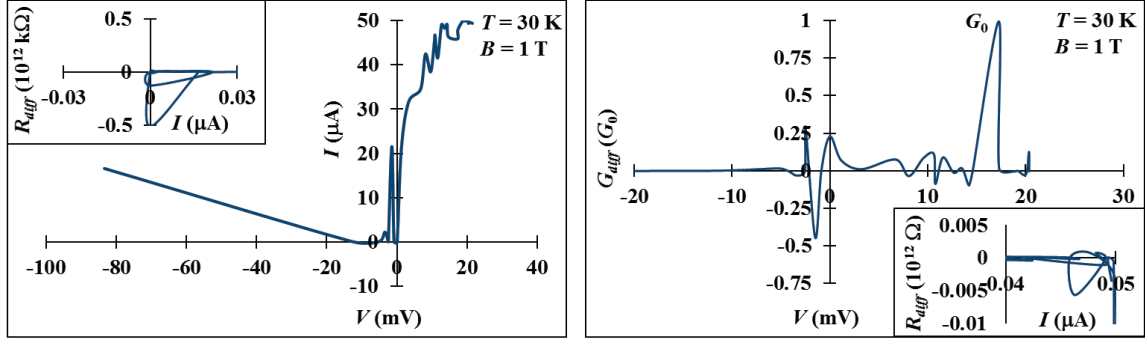
Figure 4 Nonlinear current-voltage characteristic $I(V)$ and the corresponding $G_{diff}(V)$ data for O-implanted (at 2.24×10^{16} ions/cm^2) C fiber in transverse magnetic field.

3.2.2 Colossal magnetoresistance

Low-temperature magnetoresistance $MR(\%) = 100 \times [R(B) - R(B=0)]/R(B=0)$
for a C fiber O-implanted at 2.24×10^{16} ions/cm^2 is shown in Figure 5. While MR takes colossal values for both small (50 nA) and large (50 μA) currents, the electronic charge transport is significantly less viscous for the former ($MR < 0$) than for the the latter (($MR > 0$). Viscosity generates vorticity, arguable playing the same role as the zero-electrical resistance does for SC [8].
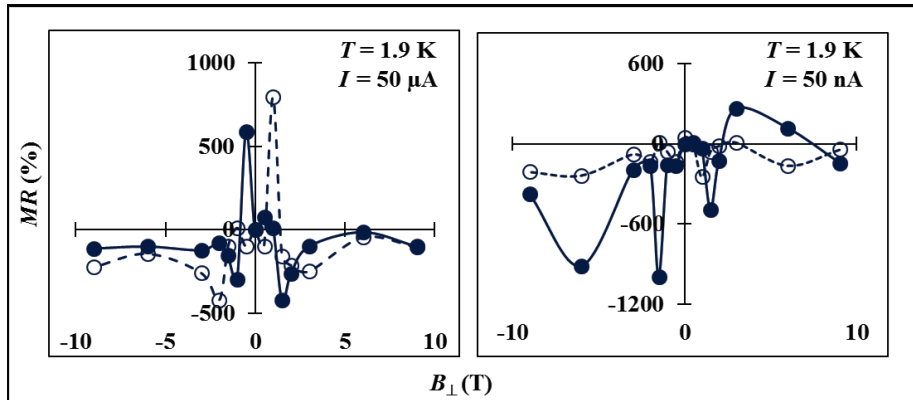

Figure 5 Magnetoresistance data for a C fiber O-implanted at 2.24×10^{16} ions/cm^2 at $T = 1.9$ K. Legend: open/closed symbols for decreasing/increasing the magnetic field with the sample thermally stabilized.

3.2.3 Andreev oscillations

We have also observed Andreev oscillations in the magnetoresistance of highly oriented pyrolytic graphite (HOPG) cylindrical samples of radius $R = 3$ mm and height 1 mm (Figure 6). While this kind of quantum resonances that are attributed to Andreev reflections between SC and semiconducting regions have been observed before [3,12], their period was significantly larger (0.1 T to 0.4 T). Here, the period for Andreev oscillations is $\Delta B = 2$ mT. We can estimate the area for the SQUID-type oscillations of two SC pathways separated by a normal/insulating region as $S = \Phi_0/\Delta B \cong 1.0 \times 10^{12}$ m^2, where $\Phi_0 \cong 2.07 \times 10^{-15}$ T·m^2 is the magnetic flux quanta. Given the sample's symmetry, this would give a radius $R \cong 560$ nm for the circular paths.
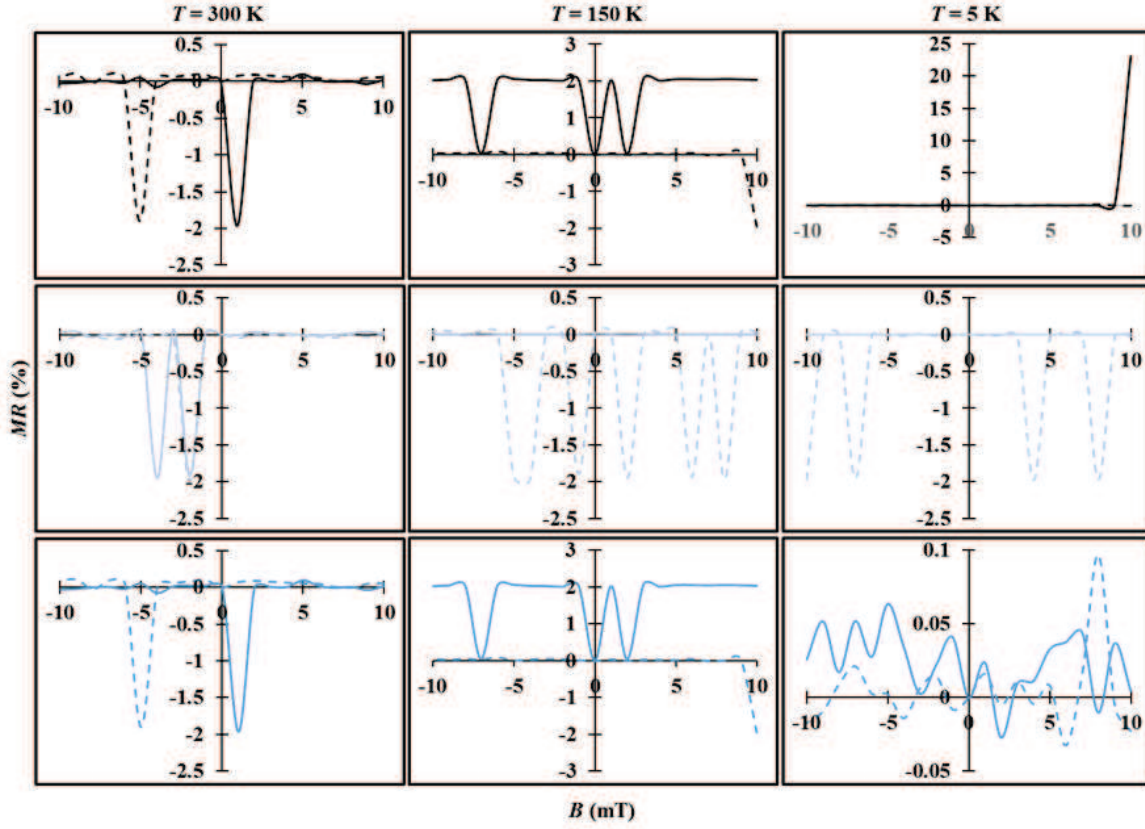
4

Figure 6 Andreev oscillations in the magnetoresistance of highly oriented pyrolytic graphite cylindrical samples O-implanted at 7.07×10^{12} ions/cm^2 (light blue), 5.66×10^{15} ions/cm^2 (blue), and raw sample (in black) at temperatures 5 K, 150 K, and 300 K, respectively.

3.3 Magnetization measurements
3.3.1 Zero-field cooled (ZFC) and field-cooled (FC) measurements
Temperature-dependent ZFC-FC magnetization data for O-implanted graphite foil samples having dimensions 2 mm × 2 mm × 1 mm are shown in Figure 7. While fluctuations are observed up to $T \sim$ 150 K, the irreversibility temperature is $T_{irrev} \cong 50 - 60$ K. Our results are close to the BCS mean-field calculations that found the critical temperature T_c for graphite at 60 K [13] and for graphene at 150 K [9]. An unusual feature is the upward turn of the magnetization at low temperatures that was interpreted as a "reentry" phenomena [14]. The magnetization in the SC phase has three sources: (a) the diamagnetic shielding moment, (b) the trapped flux and (c) a paramagnetic contribution (positive magnetic susceptibility χ_m) from the normal matrix. The $T_{irrev} \sim 50$ K here obtained is the same as the estimate of T_c for semiconducting structures [16], where the excitonic mechanism was proposed [15].
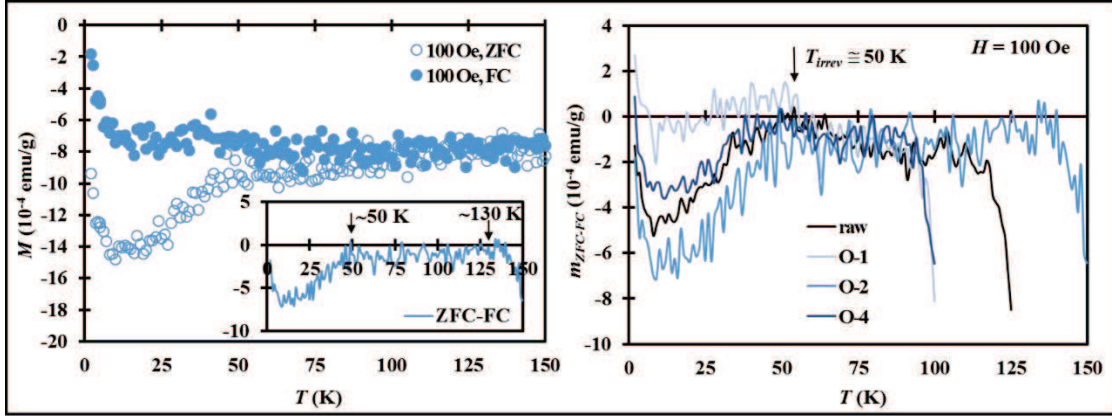
Figure 7 Zero-field cooled (ZFC) and field-cooled (FC) temperature dependent magnetization data for graphite foil samples O-implanted at 2D concentrations 7.07×10^{12} ions/cm^2 (O-1), 5.66×10^{15} ions/cm^2 (O-2), and 2.24×10^{16} ions/cm^2 (O-3). Data for a raw sample is also shown.

3.3.2 Magnetization loops

Magnetic-field dependent magnetization loops at $T = 300$ K for the described before graphite foil samples are shown in Figure 8. Except for the prolonged tail, these high-temperature magnetization loops are clearly similar to the ones found for hard SCs. In addition, these loops also show the kink characteristic to granular SCs such as the ones found in [16]. Low-field loops (Figure 9a) show the shielding effect due to the pseudo-Meissner effect [17]. The $M(H)$ loops for HOPG and graphite samples are similar (Figure 9b). The magnetic coherence length $\xi_m = \left(\frac{\Phi_0}{2\pi B_{c2}}\right)^{1/2}$ is in the $100 - 200$ nm range.
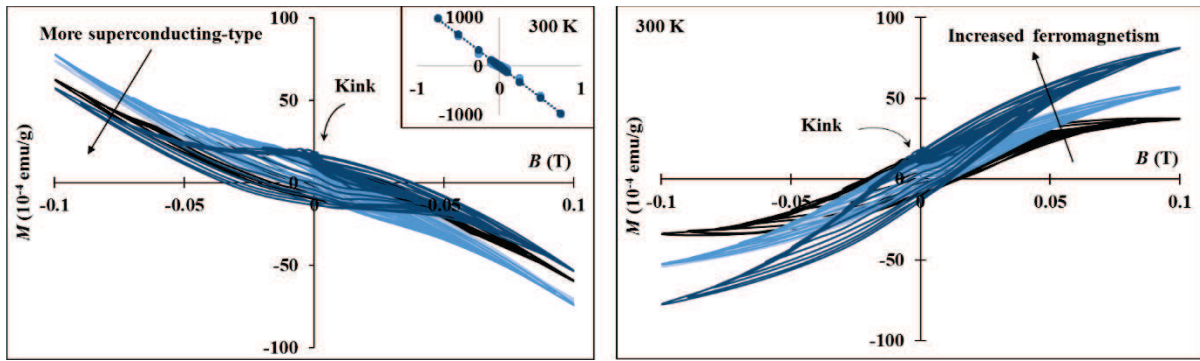

Figure 8 Nonlinear and irreversible $M(B)$ loops at $T = 300$ K for O-implanted graphite foil samples: raw (in black) and O-implanted (in blue, description in Figure 7) before (left) and after (right) the subtraction of their own diamagnetic background (inset).
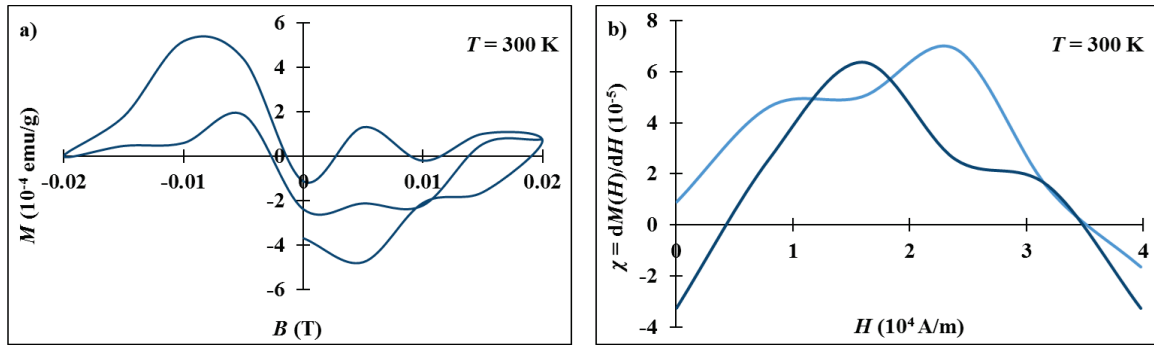
Figure 9 a) Superconducting-type magnetization loop for a graphite foil sample (O-ion implantation dose 5.64 x 10^{15} ions/cm^2). b) Field-dependence of the magnetic susceptibility χ for an O-implanted sample at 2.24 x 10^{16} ions/cm^2 (in dark blue) and for an O-implanted (at 5.64 x 10^{15} ions/cm^2) graphite foil sample (in blue).

4. Conclusions

Graphitic materials are extremely rich in quantum phenomena. In this work, we have presented experimental evidence for Andreev reflections, colossal magnetoresistance, ferromagnetism and granular superconducting-like behaviour. Future work will explore in more detail these and other related phenomena.

5. References

[1]   D. Spemann, P. Esquinazi, R. Höhne, A. Setzer, M. Diaconu, H.Schmidt, T. Butz 2005 Magnetic carbon: A new application for ion microbeams *Nuclear Instruments and Methods in Physics Research B* **231(1-4)** 433

[2]   T.L. Makarova *et al*. 2015 Edge state magnetism in zigzag-interfaced graphene via spin susceptibility measurements *Scientific Reports* **5** 13382

[3]   P. Esquinazi *et al*. 2008 Indications for intrinsic superconductivity in highly oriented pyrolytic graphite *Phys. Rev. B* **78** 134516

[4]   Y. Cao *et al*. 2018 Correlated insulator behaviour at half-filling magic angle graphene superlattices, *Nature* **80** 56

[5]   B.T. Pierce, J.L. Burke, L.B. Brunke, T.J. Bullard, D.C. Vier, and T.J. Haugan 2013 Search for Superconductivity in Doped Amorphous Carbon Thin Films *IEEE Transactions on Applied Superconductivity* **23(3)** 7000205

[6]   J.W. Ekin 2006 Experimental Techniques for Low-temperature measurements *Oxford University Press*

[7]   I.L. Spain, K.J. Volin, H.A. Goldberg, and I.L. Kalnin 1983 Unusual electrical resistivity behavior in carbon fibers *Solid State Commun*. **45(9)** 817

[8]   L. Levitov and G. Falkovich 2016 Electron viscosity, current vortices and negative nonlocal resistance in graphene *Nat. Phys.* **12** 672

[9]   D.V. Kveshchenko 2009 Massive Dirac fermions in single-layer graphene *J. Phys.: Condes. Matter* **21(7)** 075303

[10] N.V. Stankevich, N.V. Kuznetsov, G.A. Leonov, and L.O. Chua 2017 Scenario of the Birth of Hidden Attractors in the Chua Circuit *International Journal of Bifurcation and Chaos* **27(12)** 1730038

[11] I.A. Korneev, and V.V. Semenov 2017 Andronov–Hopf bifurcation with and without parameter in a cubic memristor oscillator with a line of equilibria *Chaos* **27** 081104

[12] J. Ridderbos,et al. 2019 Multiple Andreev reflections and Shapiro steps in a Ge-Si nanowire Josephson junction *Phys. Rev. Materials* **3** 084803

[13] N. García and P. Esquinazi 2009 Mean Field Superconductivity Approach in Two Dimensions *J*

Supercond Nov Magn **22** 439

[14]   Y. Yeshurun, I. Felner, and H. Sompolinski 1987 Magnetic properties of a high-T_c superconductor YBa$_2$Cu$_3$O$_7$: Reentrylike features, paramagnetism, and glassy behavior *Phys. Rev. B* **36(1)** 840

[15] E.D. Cherotchenko, T. Espinosa-Ortega, A.V. Nalitov, I.A. Shelykh, A.V. Kavokin 2016 Superconductivity in semiconductor structures: The excitonic mechanism *Superlattices and Microstructures* **90** 170

[16] S. Saha and B.K. Das 1993 A realistic two-component critical state model: successful derivation of low-field M-H loops of granular superconductors *Supercond. Sci. Technol.* **6** 685

[17] M.D. Sumption, E. Lee, E.W. Collings, X.L. Wang, and S.X. Dou 2002 Suppression of AC (hysteretic) loss of magnetic shielding of MgB$_2$/Fe superconductors: The pseudo-Meissner effect *Advances in Cryogenic Engineering: Proceedings of the International Cryogenic Materials Conference* **48A and B** *AIP Conference Proceedings* **614** 824